Physica D 36 (1989) 222–234
North-Holland, Amsterdam

ANALYSIS OF A SIX-COMPONENT ATMOSPHERIC SPECTRAL MODEL: CHAOS, PREDICTABILITY AND VACILLATION

H.E. DE SWART*
Centre for Mathematics and Computer Science, P.O. Box 4079, 1009 AB Amsterdam, The Netherlands

Received 9 March 1988
Revised manuscript received 15 January 1989
Accepted 17 February 1989
Communicated by A.V. Holden

The properties of a low-order atmospheric spectral model are investigated by using a bifurcation analysis of its steady states and periodic solutions. The time-asymptotic behaviour of the model is either stationary, periodic, quasi-periodic or chaotic, depending on the parameter values and initial conditions. Different scenarios are found leading to the generation of strange attractors. Some include the occurrence of homoclinic orbits, such that for nearby parameter values chaotic orbits exist moving in small tubes around the homoclinic orbits. The chaotic motion describes an irregular flow, predictable on a time scale given by the reciprocal of its positive Lyapunov exponent. However, the model cannot describe transitions between different preferent flow regimes. This is due to the severe truncation of the spectral expansions.

1. Introduction

Largely due to the work of Lorenz [1] it is nowadays accepted that the atmosphere is a physical system with limited predictability properties. Consequently, weather forecasts only have validity on a finite time interval, which appears to be two weeks at most. As indicated by model results as well as data, another characteristic property of the system is its vacillation behaviour: the circulation irregularly fluctuates between different preferent flow regimes (also called weather regimes). Often they are classified into three categories: a high-index regime (intense westerlies, small wave amplitudes), a low-index regime (large waves, weak zonal flow) and an intermediate regime of transitional type. More details and extensive references are given in [2]. These properties cannot be explained by a linear theory: they are a consequence of the nonlinear interactions between different scales of motion. Within the framework of long-term weather forecasting it is important to obtain a better understanding of the dynamics responsible for the features reported above.

In this paper the possibility of constructing simple nonlinear models, which reflect the vacillation and predictability properties of the atmosphere, is investigated. This is done by a Galerkin projection of the equations of motion onto a limited number of normal modes of the system. The result is a spectral model

$$\dot{\boldsymbol{x}} = \boldsymbol{f}_{\mu}(\boldsymbol{x}) \quad \text{in } \mathbb{R}^N. \tag{1.1}$$

Here $\boldsymbol{x} = (x_1, x_2, \ldots, x_N)$ represents the modal amplitudes, an overdot denotes differentiation with respect

*Present address, Institute of Meteorology and Oceanography, University of Utrecht, Princetonplein 5, 3584 CC Utrecht, The Netherlands.

to time and $f_\mu(x)$ is an N-dimensional vector field depending on x and parameters $\mu = (\mu_1, \mu_2, \ldots, \mu_m)$. Furthermore, N is the truncation number and $\mathbb{R}^N$ the phase space.

In this paper we shall study a six-component spectral model of the barotropic potential vorticity equation in a beta plane channel. It was originally derived by Charney and DeVore [3] and is also considered in [4]. Although these studies answered many questions, our knowledge of the model is still incomplete. In particular the existence of vacillatory solutions has not been investigated. Therefore we shall investigate whether this model contains a strange attractor with an associated multimodal probability distribution in the phase space. Since the chaotic motion is characterized by sensitive dependence on initial conditions, it models a finitely predictable flow. The multimodal probability distribution means that the trajectories alternately visit different preferent regions in the phase space, as required to simulate vacillation behaviour.

After a brief derivation of the spectral equations in section 2, we study in section 3 the steady-state structure of the model. The two parameters varied are the external forcing, controlling the topographic instability mechanism, and the width–length ratio of the channel with which the barotropic triad interactions are controlled. The existence of strange attractors is investigated in sections 4 and 5 by continuing in the parameter space branches of periodic orbits which bifurcate from the steady states. In some cases the periodic orbits become homoclinic, such that they connect unstable equilibria with themselves. For nearby parameter values strange attractors occur, in agreement with Silnikov's theory [5], see also [6, 7]. However, although the model has interesting properties it cannot represent the vacillation behaviour of the atmospheric circulation. This is due to the lack of sufficient nonlinear interactions, caused by the severe truncation of the spectral equations. It is argued in section 6 that more degrees of freedom are needed to obtain the vacillation behaviour.

2. The model

The spectral model equations are derived as follows (see [2] for details and references). Consider a large-scale atmospheric flow (length scale k^{-1}, time scale σ^{-1}, scale height H) on a beta plane centered at latitude $\phi = \phi_0$ of the spherical earth. The dynamics of this type of flow are governed by the nondimensional vorticity equation

$$\frac{\partial}{\partial t}\nabla^2\psi + J(\psi, \nabla^2\psi) + \gamma J(\psi, h) + \beta\frac{\partial\psi}{\partial x} + C\nabla^2(\psi - \psi^*) = 0. \tag{2.1}$$

Here t is time, $\psi(x, y, t)$ the stream function, $h(x, y)$ represents the topography of the earth (characteristic amplitude h_0) and $\psi^*(x, y)$ is a forcing stream function modelling the equator to pole temperature difference. All variables have been nondimensionalized according to the scales given above. Furthermore, ∇^2 is the two-dimensional Laplace operator and

$$J(a, b) = \frac{\partial a}{\partial x}\frac{\partial b}{\partial y} - \frac{\partial a}{\partial y}\frac{\partial b}{\partial x}, \quad \mathrm{d}x = kr_0\cos\phi_0\,\mathrm{d}\lambda, \quad \mathrm{d}y = kr_0\,\mathrm{d}\phi, \tag{2.2}$$

where λ is the longitude, ϕ the latitude and r_0 the radius of Earth. The parameters are

$$\gamma = \frac{f_0 h_0}{\sigma H}, \quad \beta = \frac{\beta_0}{\sigma k}, \quad C = \frac{f_0\delta_E}{2\sigma H}, \tag{2.3}$$

with $f_0 = 2\Omega \sin\phi_0$, $\beta_0 = (2\Omega/r_0)\cos\phi_0$, Ω the angular speed of rotation of Earth and δ_E the depth of the frictional (Ekman) boundary layer near the Earth's surface. The motion is considered in a rectangular channel with the boundary conditions

$$\psi(x, y, t) = \psi(x + 2\pi, y, t),$$
$$\frac{\partial \psi}{\partial x} = 0 \quad \text{and} \quad \frac{\partial}{\partial t}\int_0^{2\pi} \frac{\partial \psi}{\partial y}\, dx = 0 \quad \text{at } y = 0,\ y = \pi b\ (= 2\pi B/L), \tag{2.4}$$

where B and L are the dimensional width and length of the channel, respectively.

Next the solution ψ is expanded in a series of orthonormal eigenfunctions $\{\Phi_j\}_j$ of the Laplace operator. Assuming that ψ^* and h can be expanded in eigenfunctions as well, we have

$$(\psi, \psi^*, h) = \sum_j (\psi_j, \psi_j^*, h_j)\Phi_j, \quad j = (j_1, j_2), \tag{2.5}$$

where j_1 and j_2 are integers and we require each mode (ψ_j, Φ_j) to satisfy the boundary conditions (2.4). In this case we find

$$\Phi_{0j_2} = \sqrt{2}\cos(j_2 y/b), \quad \Phi_{j_1 j_2} = \sqrt{2}\exp(\mathrm{i}\, j_1 x)\sin(j_2 y/b), \quad |j_1|,\ j_2 = 1, 2, \ldots. \tag{2.6}$$

They represent $(0, j_2)$ zonal flow modes and $(|j_1|, j_2)$ Rossby wave modes, respectively.

A low-order model is constructed by letting $(-1, 1) \le \boldsymbol{j} \le (1, 2)$. The topography and external forcing are represented by

$$h = \cos(x)\sin(y/b), \quad \psi^* = \sqrt{2}\psi_{01}^* \cos(y/b). \tag{2.7}$$

Projecting eq. (2.1) on these eigenfunctions and introducing the real-valued velocity amplitudes

$$\begin{aligned} x_1 &= \psi_{01}/b, & x_1^* &= \psi_{01}^*/b, \\ x_2 &= (\psi_{11} + \psi_{-11})/(\sqrt{2}b), & x_3 &= \mathrm{i}(\psi_{11} - \psi_{-11})/(\sqrt{2}b), \\ x_4 &= \psi_{02}/b, & & \\ x_5 &= (\psi_{12} + \psi_{-12})/(\sqrt{2}b), & x_6 &= \mathrm{i}(\psi_{12} - \psi_{-12})/(\sqrt{2}b), \end{aligned} \tag{2.8}$$

we obtain the spectral equations

$$\begin{aligned} \dot{x}_1 &= \gamma_1^* x_3 - C(x_1 - x_1^*), \\ \dot{x}_2 &= -(\alpha_1 x_1 - \beta_1)x_3 - Cx_2 && -\delta_1 x_4 x_6, \\ \dot{x}_3 &= (\alpha_1 x_1 - \beta_1)x_2 - \gamma_1 x_1 - Cx_3 && +\delta_1 x_4 x_5, \\ \dot{x}_4 &= \gamma_2^* x_6 - Cx_4 && +\varepsilon(x_2 x_6 - x_3 x_5), \\ \dot{x}_5 &= -(\alpha_2 x_1 - \beta_2)x_6 - Cx_5 && -\delta_2 x_3 x_4, \\ \dot{x}_6 &= (\alpha_2 x_1 - \beta_2)x_5 - \gamma_2 x_4 - Cx_6 && +\delta_2 x_2 x_4. \end{aligned} \tag{2.9}$$

Here

$$\alpha_m = \frac{8\sqrt{2}}{\pi}\frac{m^2}{4m^2-1}\frac{b^2+(m^2-1)}{b^2+m^2}, \qquad \beta_m = \frac{\beta b^2}{b^2+m^2},$$
$$\delta_m = \frac{64\sqrt{2}}{15\pi}\frac{b^2-(m^2-1)}{b^2+m^2}, \qquad \gamma_m^* = \frac{4m}{4m^2-1}\frac{\sqrt{2}\,b\gamma}{\pi}, \tag{2.10}$$
$$\varepsilon = \frac{16\sqrt{2}}{5\pi}, \qquad \gamma_m = \frac{4m^3}{4m^2-1}\frac{\sqrt{2}\,b\gamma}{\pi(b^2+m^2)}$$

are functions of the model parameters. This model is identical to that discussed in [3, 4], except for a different scaling.

Note that the model is invariant under reflection in $x_4 = x_5 = x_6 = 0$. This implies that if initial conditions are chosen such that $x_4(0) = x_5(0) = x_6(0) = 0$, the evolution is governed by the three-component subsystem in (2.9) between the solid lines. Its properties are simple and well-known [2, 3]. For a wide range of parameter values it possesses three different equilibria (E_1, E_2, E_3). Here E_1 and E_3 are stable, whereas E_2 is unstable due to the topographic instability mechanism. The corresponding stream function patterns resemble the three large-scale preferent regimes of the atmospheric circulation reported in the introduction. However, no vacillation behaviour is found.

Compared with this three-component model, the full model (2.9) exhibits a new physical mechanism, called the barotropic instability. This is caused by the triad interactions between the (0,2), (1,1) and (1,2) modes. Application of the Fjørtoft theorem [8] to this triad yields

$$\begin{aligned} &\text{if } b^2 < 3: \quad (0,2) \text{ mode can become unstable,} \\ &\text{if } b^2 > 3: \quad (1,1) \text{ mode can become unstable.} \end{aligned} \tag{2.11}$$

We shall study the set of limit points of (2.9) for the parameter values $C = 0.1$, $\beta = 1.25$, $\gamma = 1$ and b and $x_1^* = Uk/\sigma$ free. Here U is the external velocity forcing in the (0,1) mode and $\sigma/k = 8$ m s^{-1}. The situation is that of a flow confined to a channel with length 5000 km and variable width, centered at the latitude $\phi_0 = 45°$. Furthermore, the topographic amplitude is 1 km and the dissipation time scale 10 days. The model has been analyzed by using routines from the software package AUTO of Doedel [9], in combination with numerical time integrations.

3. Stationary solutions and their bifurcations

Concerning the equilibria of (2.9), we distinguish between single-mode equilibria, for which the x_4-, x_5- and x_6-components are zero, and the other mixed-mode equilibria. The latter always occur in pairs, due to the reflection symmetry of the model. In fig. 1 curves in the (b, x_1^*) parameter space are shown, where one or more real parts of the eigenvalues of the vector field, linearized at a stationary point, become zero. The solid curves L1, L2 and L3 are curves of limit points (saddle–node bifurcations). The dashed lines are curves of ordinary bifurcation points, whereas the dotted lines, labelled H1, H2 and H3, are curves of Hopf bifurcation points. At the limit points and bifurcation points two branches of equilibria come together. Consequently, the associated curves in fig. 1(a) divide the parameter space into regions, each with its own characteristic number of equilibria. This is denoted by the symbols a_s, a_m, where a_s represents the

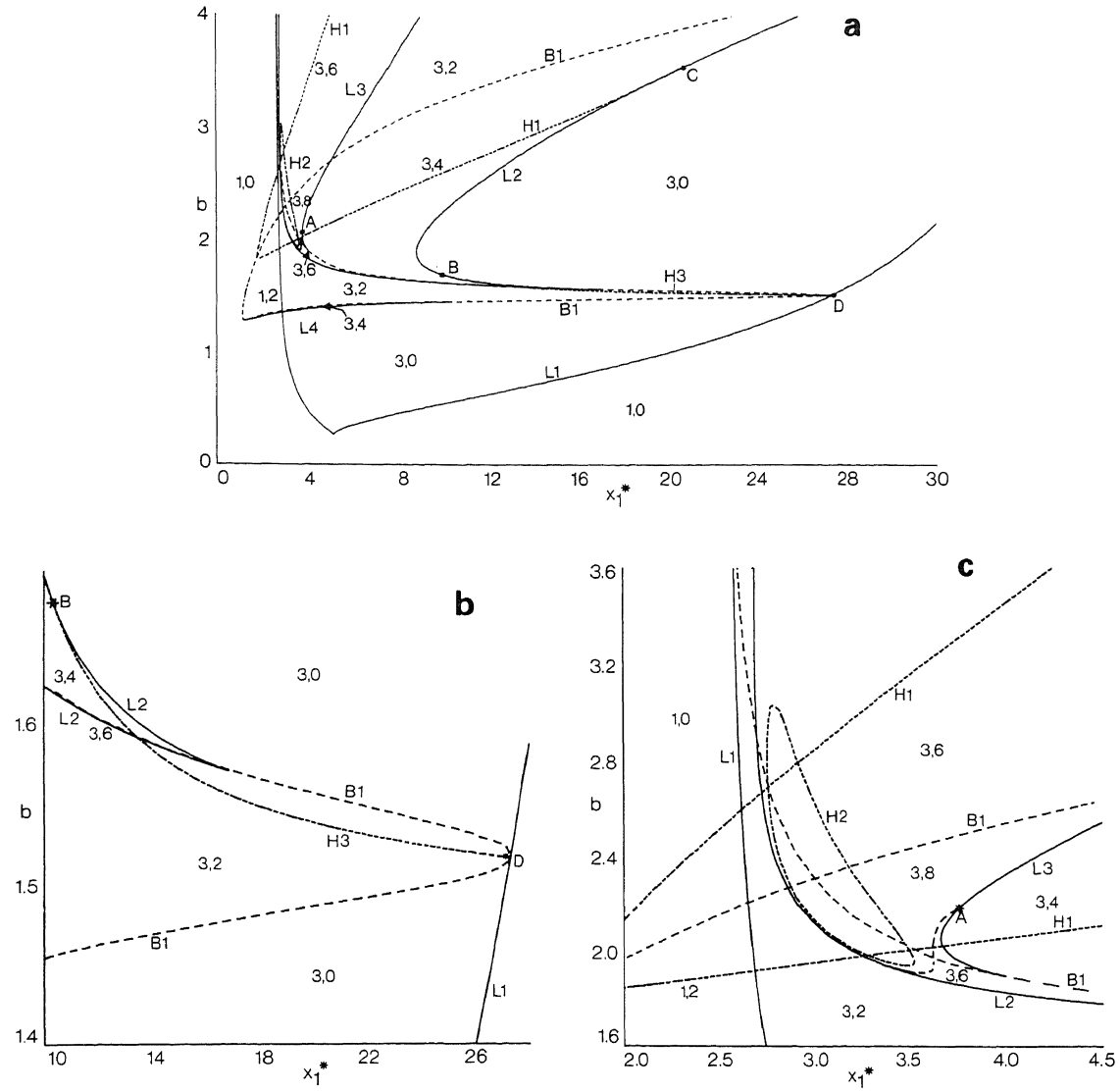

Fig. 1. (a) Curves of singular points in the (b, x_1^*) parameter space. Solid lines are curves of limit points (L1, L2, L3), dashed lines are curves of pitchfork bifurcations (B1) and dotted lines are curves of Hopf bifurcation points (H1, H2, H3). The symbols a_s, a_m denote the number of single-mode and mixed-mode equilibria, respectively. The points A, B, C and D are associated with a direct transition from regular to chaotic behaviour. (b) Blow-up of (a) near point *D*. (c) Blow-up of (a) near point *A*.

number of single-mode equilibria and a_m the number of mixed-mode equilibria. Stability properties of at least one of the equilibria change each time that a curve in the diagram is crossed. They are not indicated, since the diagram is already densely filled with information. In fig. 1(b, c) blow-ups of two regions are presented where the behaviour is rather complicated. Thick points in the diagram are special singular points of the model, because they are associated with bifurcations of codimension larger than one. Of particular interest are the points A, B, C and D, where we have the coalescence of a Hopf bifurcation and saddle–node bifurcation. At these points a direct transition occurs from regular to chaotic solutions [10]. They suggest the existence of homoclinic orbits and related chaos, which will be investigated in more detail

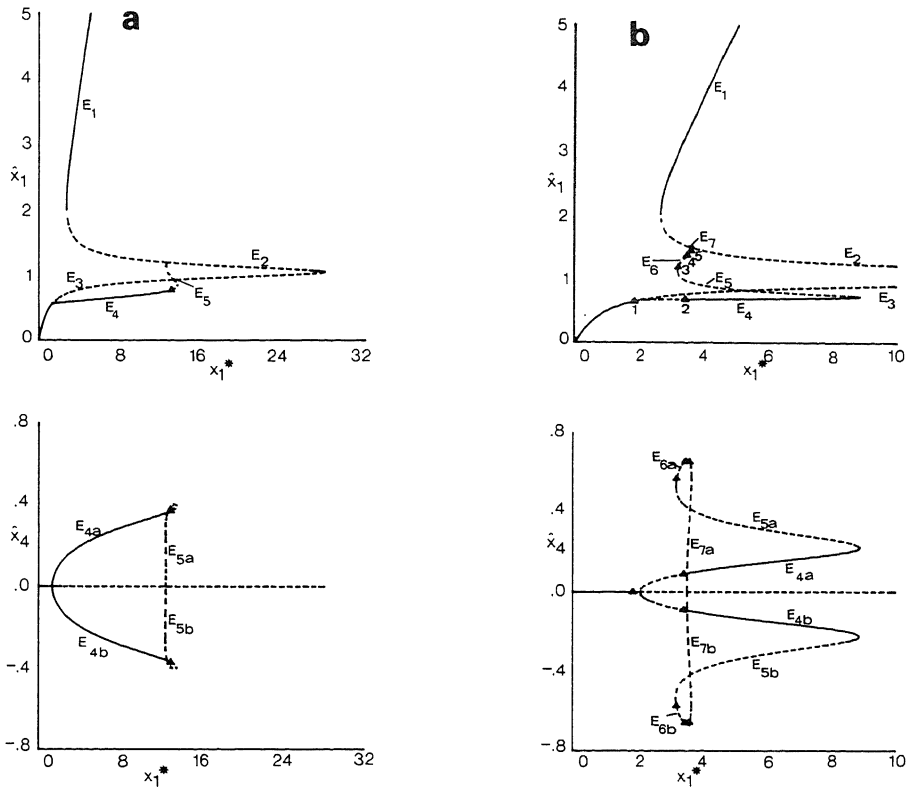

Fig. 2. x_1- and x_4-component of the equilibria as a function of x_1^* for $b = 1.6$ (a) and $b = 2$ (b). A solid line denotes that the solution is stable, whereas a dashed line indicates an unstable solution. The triangle symbols denote Hopf bifurcation points, which are numbered accordingly in (b).

in the next section.

The curve L1 is the bifurcation set of the three-component subsystem. From fig. 1 we conclude that for $b < 1.279$ the six-component model has only single-mode equilibria. If b becomes larger, additional mixed-mode equilibria may occur. If b exceeds the value 1.517, periodic solutions may be generated due to the presence of Hopf bifurcations, being a manifestation of the barotropic instability mechanism. In fig. 2 cross-sections of the bifurcation diagram are presented. Shown are the x_1- and x_4-component of the equilibria as a function of x_1^* for $b = 1.6$ and $b = 2$. Note that the high-index equilibria (E_1) are always stable, as will be used later on.

4. Periodic and aperiodic solutions

4.1. *Zonal flow instabilities*

We have studied the position and stability of periodic orbits branching off from stationary points as a function of the forcing parameter x_1^*. This has been done for the cases $b = 1.6$ and $b = 2$, which are characteristic for the behaviour of the model, as is indicated by (2.11). Note that once the periodic orbits

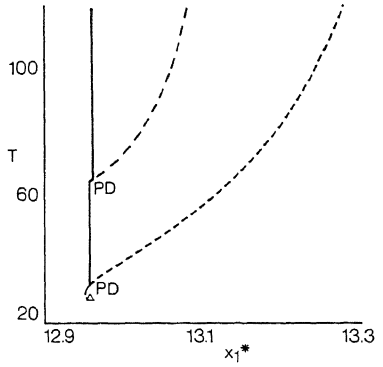

Fig. 3. Period T of periodic orbits as a function of x_1^* for $b = 1.6$. Stability properties are denoted by a solid curve (stable) or a dashed curve (unstable). A Hopf bifurcation is indicated by a triangle symbol, a period-doubling bifurcation by PD.

branch off from stationary points of the mixed-mode type, they occur in pairs. Again this is a consequence of the reflection symmetry present in eq. (2.9).

For $b = 1.6$ one pair of Hopf bifurcation points is found at mixed-mode equilibrium branches, see fig. 2(a). The result of the continuation of the periodic orbits, emanating from this point, as a function of x_1^* is presented in fig. 3. The branch of initially unstable periodic orbits almost immediately merges into a saddle–node bifurcation. As a result stable periodic solutions are found in a small range of x_1^*-values, of which an example is shown in fig. 4(a). However, they soon become unstable due to a sequence of period-doubling bifurcations, leading to the generation of a strange attractor. An example of an associated chaotic orbit is shown in fig. 4(b). By application of the method described in Wolf et al. [11] one positive Lyapunov exponent $\nu_1 = 0.016$ was computed for this signal. The reciprocal of this number gives the time scale on which the motion is predictable on the average. We have not analyzed the strange attractors in detail, since they do not have a global structure: chaotic solutions permanently remain in the low-index flow regime. Moreover, it appears that for slightly larger x_1^*-values they turn into nonattracting strange invariant sets. These qualitative changes are associated with global bifurcations involving heteroclinic connections between the unstable periodic orbits and the saddle points E_{5a}/E_{5b} defined in fig. 2(a). The strange invariant sets disappear in a global bifurcation at $x_1^* \approx 13.36$. For that parameter value the periodic orbits have become homoclinic, connecting E_{5a} and E_{5b} with themselves. A numerical approximation of one of the homoclinic orbits, considered as a periodic orbit with period $T \to \infty$, is shown in fig. 4(c). This scenario is described in [12] as a type-B homoclinic explosion.

4.2. *Rossby wave instabilities*

We now consider the situation $b = 2$, for which five different Hopf bifurcation points have been found, numbered accordingly in fig. 2(b). In fig. 5 the period of the orbits emanating from the Hopf bifurcations 1 (a) and 2 (b) is shown as a function of x_1^*. Part of the diagram on the left is also discussed in [4]. Clearly, the bifurcation structure is complicated: we observe symmetry-breaking and symmetry-recovering pitchfork bifurcations as well as period-doubling and period-halving bifurcations. However, the most interesting property in both diagrams is the tendency of the period to become infinitely large as x_1^* tends to the value 3.581 (fig. 5(a)) or 3.584 (fig. 5(b)). This behaviour corresponds to the approach to homoclinic orbits connecting the saddle-point E_3 with itself. Numerical approximations of these orbits are shown in

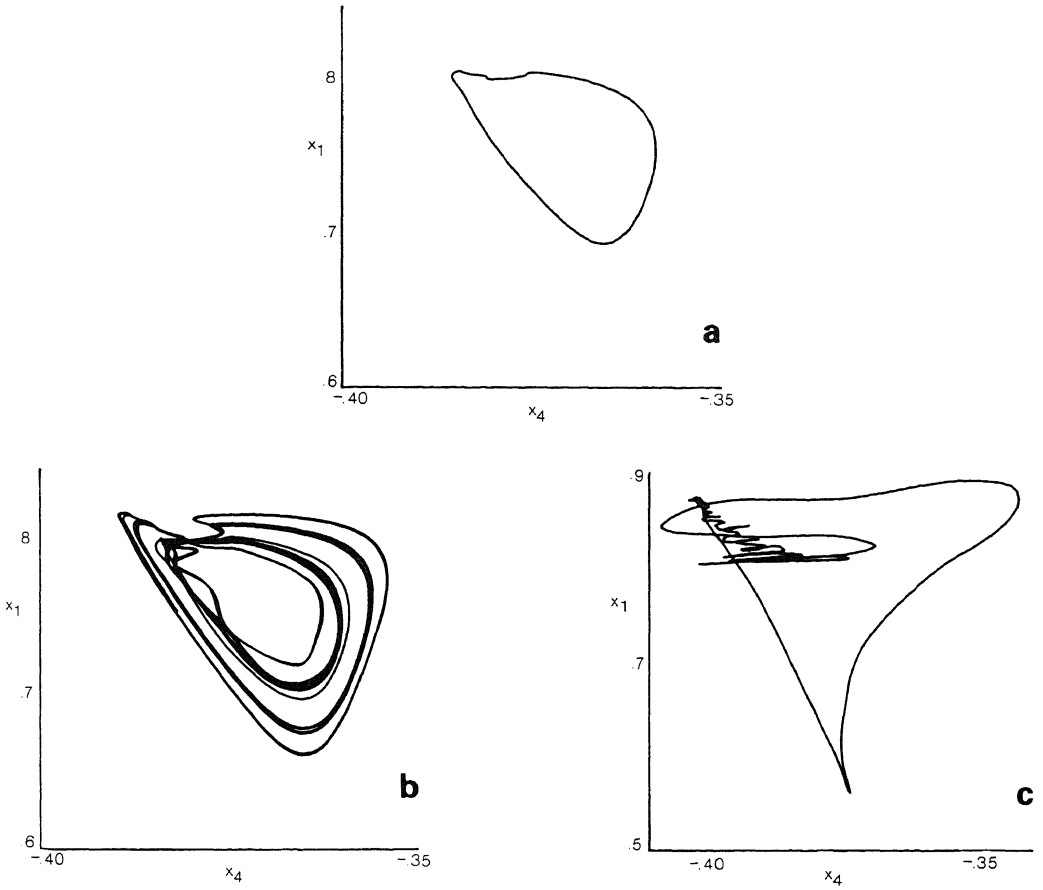

Fig. 4. (a) Projection of a periodic orbit, existing for $b = 1.6$ and $x_1^* = 12.958$, on to the x_1–x_4 plane. (b) Projection of a chaotic orbit, existing for $b = 1.6$ and $x_1^* = 12.961$, on to the x_1–x_4 plane. (c) Numerical approximation of one of the two homoclinic orbits occurring at $b = 1.6$ and $x_1^* = 13.36$ as a periodic solution with period $T \to \infty$. Shown is the projection of the orbit on to the x_1–x_4 plane. The other orbit is obtained by reflection in $x_4 = x_5 = x_6 = 0$.

fig. 6(a, b). Note that each of the two asymmetric orbits seems to be just half a part of the homoclinic orbit presented in fig. 6(a).

This type of bifurcation has been analyzed in [5–7]. The local behaviour of the vector field near a homoclinic orbit is characterized by three eigenvalues of the matrix derivative of the vector field linearized at the saddle point. They are a real positive eigenvalue λ_1 and two complex-conjugated eigenvalues $(-\lambda_2 \pm i\omega)$, with $\lambda_2 > 0$ and $\lambda_2/\lambda_1 < 1$. It follows that for parameter values close to homoclinicity strange attractors exist, which occur and disappear due to cascades of period-doubling and period-halving bifurcations, respectively. These bifurcations take place near each winding of the $T(x_1^*)$ curves of fig. 5. An example of a chaotic orbit, existing for $x_1^* = 3.5$, is shown in fig. 6(c). It has one positive Lyapunov exponent, $\nu_1 = 0.040$. Note that the trajectories move in small tubes which closely resemble the homoclinic orbit of fig. 6(a).

Apart from the principal homoclinic orbit there may exist a number of others, the so-called principal homoclinic orbits, which make one or more encounters with the saddle points before returning to them. Suppose that the saddle–node bifurcations, associated with the approach to an M-pulse homoclinic orbit

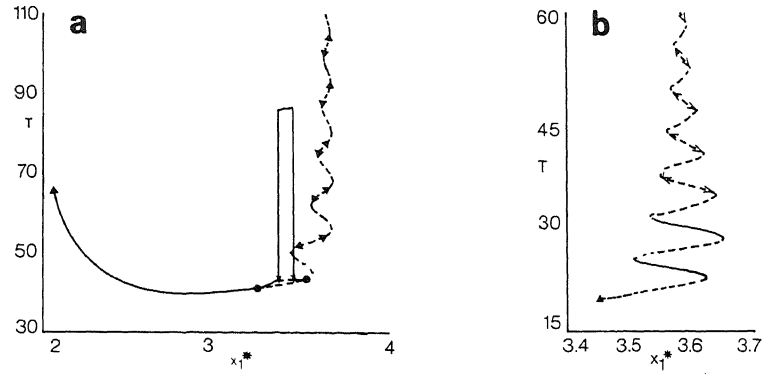

Fig. 5. Period T of periodic orbits emanating from the Hopf bifurcation points labelled 1 (a) and 2 (b) in fig. 2b as a function of x_1^*. Stability properties are indicated by a solid curve (stable) and a dashed curve (unstable). The triangle symbol denotes a Hopf bifurcation, • a pitchfork bifurcation and * a period-doubling bifurcation. The symbols < and > indicate a supercritical and subcritical sequence of period-doubling bifurcations in a very small range of x_1^*-values.

occurring for the parameter value μ_{0M} are found for the parameter values μ_i $(i = 1, 2, \ldots, \infty)$ with T_i the corresponding periods of the orbits. Then [6] show that

$$\lim_{i\to\infty} (T_{i+1} - T_i) = \frac{M\pi}{\omega}, \tag{4.1a}$$

$$\lim_{i\to\infty} \left[\frac{\mu_{i+1} - \mu_{0M}}{\mu_i - \mu_{0M}}\right] = -\exp\left[\frac{-\pi\lambda_2}{\omega}\right]. \tag{4.1b}$$

In our model the numerical values of the three relevant eigenvalues are

$$\lambda_1 = 0.325, \quad \lambda_2 = 0.067, \quad \omega = 1.034. \tag{4.2}$$

Upon substituting in the right-hand sides of (4.1a,b) we obtain the values $3.04M$ and -0.82, respectively. From fig. 5(a,b) we computed approximations of the left-hand sides of (4.1a,b), which are presented in

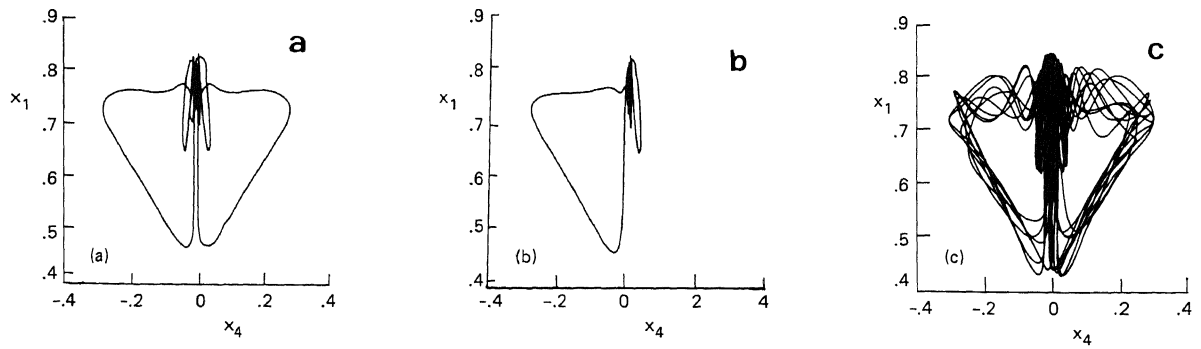

Fig. 6. (a) As fig. 4c, but approximation of the single homoclinic orbit found for $b = 2$, $x_1^* = 3.581$. (b) As fig. 4(c), but for $b = 2$, $x_1^* = 3.584$. (c) As fig. 4(b), but for $b = 2$, $x_1^* = 3.5$.

Table I
Approximations of the left-hand sides of eqs. (4.1a) and (4.1b) from the bifurcation diagrams of figs. 5(a) and 5(b).

	Fig. 5(a)	Fig. 5(b)
$T_{i+1} - T_i$	6.2	3.1
$\frac{\mu_{i+1} - \mu_{0M}}{\mu_i - \mu_{0M}}$	−0.89	−0.81

table I. From that we conclude that the two homoclinic orbits at $x_1^* = 3.584$ are principal orbits, whereas the homoclinic orbit found for $x_1^* = 3.581$ is a double-pulse subsidiary orbit.

4.3. *Bifurcation structure of the residuary periodic orbits*

The continuation of periodic orbits generated at the Hopf bifurcation points labelled 3 and 4 in fig. 2(b) is shown in fig. 7(a). Details of the bifurcation structure are presented in fig. 7(b). Starting from the points 3, strange attractors are generated in a similar way as described in section 4.1. Again they almost immediately turn unstable due to global bifurcations. The strange invariant sets disappear in cascades of period-halving bifurcations. Next the principal branches merge into saddle–node bifurcations, together with the branches of periodic orbits originating from the Hopf bifurcation points 4.

We finally investigate the periodic orbits generated at the Hopf bifurcation points labelled 5. From fig. 8 it appears that a series of wiggles is found, similar to those presented in fig. 5(a, b). However, in this case the conditions for the Silnikov scenario to apply, as discussed in [5–7], are not satisfied. In order to understand this behaviour, probably more complicated normal forms have to be developed and analyzed.

5. The possibility of vacillation behaviour

It was discussed in the introduction that an atmospheric spectral model should simulate the predictability and vacillation properties of the circulation. So far we have shown that the model (2.9) allows for

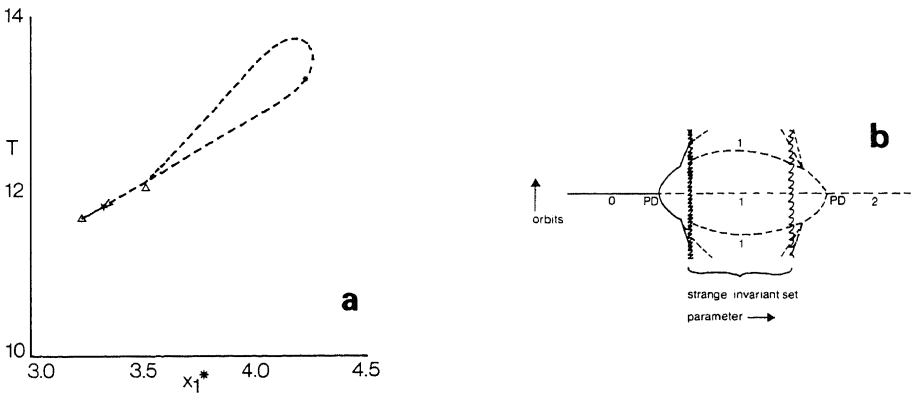

Fig. 7. (a) As fig. 5, but for the periodic orbits emanating from the Hopf bifurcation points 3 and 4. (b) Bifurcation scheme in the region between the period-doubling bifurcations (PD) of (a). The straight line represents the principal periodic orbit. The number of Floquet multipliers with absolute values larger than 1 (measuring the degree of instability of periodic orbits) is also indicated.

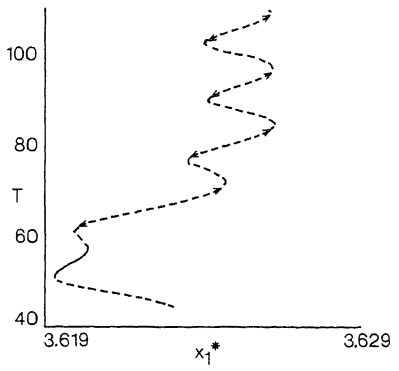

Fig. 8. As fig. 5, but for the periodic orbits emanating from the Hopf bifurcation points 5.

chaotic solutions, which are predictable for only a finite amount of time. However, the corresponding strange attractors appear to have a small size and small attraction domains, such that no vacillation is obtained. This is due to the fact that the high-index equilibrium E_1, which is dominated by a large (0,1) zonal flow modal amplitude, is stable for all parameter values. It cannot be destabilized by topographic instability, since this mechanism only acts on wave modes. Furthermore, barotropic instability of the (0,1) mode is forbidden by the Fjørtoft theorem [8] because it has the smallest wavenumber of the spectrum.

With a slight extension of the model it is possible to obtain unstable high-index equilibria. This is done by adding a forcing term Cx_4^* to the right-hand side of the equation for the evolution of the x_4-component in (2.9). In this way the (0,2) zonal flow mode of E_1 is externally forced. For sufficiently large x_4^* and $b^2 < 3$ (because of (2.11)) this mode can become barotropically unstable. As an example we take $b = 1.6$, $x_1^* = 4$ and let x_4^* be a free parameter. In fig. 9 the results of a numerical bifurcation analysis are presented. They show the x_4-components of the equilibria as a function of x_4^*, where for $x_4^* = 0$ is started in the known, previously calculated equilibria E_1, E_2 and E_3, respectively. It is obvious that E_1 becomes barotropically unstable if $|x_4^*|$ is sufficiently large. We have investigated the bifurcation structure of the periodic orbits emanating from these Hopf bifurcation points. As a result additional branches of periodic and quasi-periodic orbits were found, but no strange attractors occur. In the range $0 < |x_4^*| < 15$ trajectories either tend to a limit cycle of the high-index type or to a stationary point of the low-index type. The existence of point attractors can be understood from fig. 9(b,c). It appears that the equilibrium E_2 remains unstable if x_4^* is varied, but always a stable equilibrium of the low-index type is found. When $|x_4^*|$ is large most energy of these equilibria is contained in the (1,1) wave mode. This mode cannot become unstable because the model contains only one wave triad for which (2.11) holds, whereas here $b^2 < 3$. Thus, the conclusion is that the model (2.9) cannot simulate vacillation behaviour.

6. Conclusions

In this paper we have investigated in what sense the six-component atmospheric spectral model of ref. [3] represents predictability and vacillation properties of the atmospheric circulation. The time-asymptotic behaviour of this model is more complicated than its three-component subsystem: apart from stationary behaviour also periodic, quasi-periodic and chaotic solutions are obtained. In particular the latter are of interest, since they model an irregular time-dependent flow being predictable on a finite time interval only. However, the corresponding strange attractors do not have a global structure such that chaotic trajectories

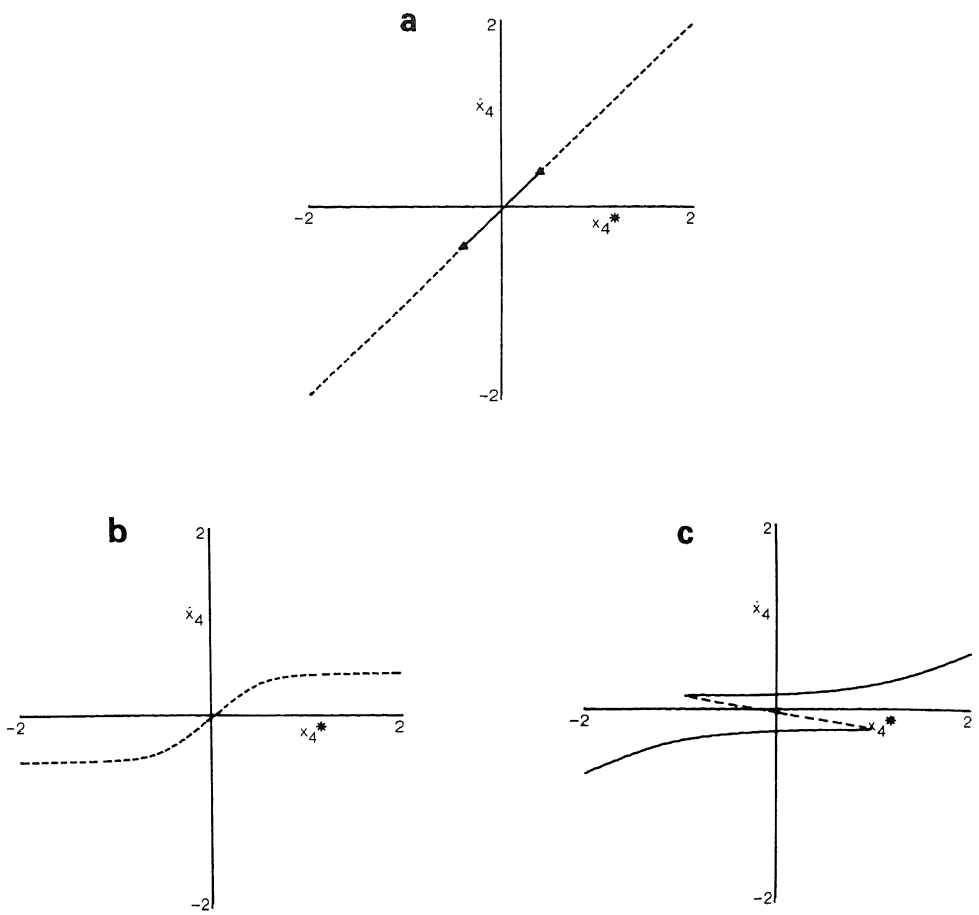

Fig. 9. x_4-components of the equilibria for $b = 1.6$ and $x_1^* = 4$ as a function of x_4^*, where for $x_4^* = 0$ is started in the known equilibrium E_1 (a), E_2 (b) and E_3 (c), respectively. Stability properties are indicated by a solid line (stable) or a dashed line (unstable). The triangle symbol denotes a Hopf bifurcation point.

are capable of visiting different preferent regions in the phase space. This is caused by the occurrence of only one barotropic triad in the model or, equivalently, by the severely truncated spectral expansions. For fixed parameter values vacillation may be generated in two different ways. The first way is to add stochastic perturbations to the model, as is done in [13]. The second one, of which examples are reviewed in [2], is to allow for more degrees of freedom by increasing the horizontal and/or vertical resolution of the spectral model.

Acknowledgements

These investigations were supported by the Technical Foundation, The Netherlands. I wish to thank Dr. J. Grasman, Dr. J.D. Opsteegh and Prof. Dr. J.T.F. Zimmerman for commenting on an earlier version of this manuscript.

References

[1] E.N. Lorenz, Tellus 21 (1969) 289.
[2] H.E. de Swart, Acta Appl. Math. 11 (1988) 49.
[3] J.G. Charney and J.G. DeVore, J. Atmos. Sci. 36 (1979) 1205.
[4] S. Yoden, J. Meteor. Soc. Japan 63 (1985) 535.
[5] L.P. Silnikov, Sov. Math. Dokl. 36 (1965) 163.
[6] D. Glendinning and C. Sparrow, J. Stat. Phys. 35 (1984) 647.
[7] P. Gaspard, R. Kapral and G. Nicolis, J. Stat. Phys. 35 (1984) 697.
[8] R. Fjørtoft, Tellus 5 (1953) 225.
[9] E.J. Doedel, AUTO 86 User Manual, Software for Continuation and Bifurcation Problems in Ordinary Differential Equations (Concordia Univ., Montreal, 1986).
[10] W.F. Langford, in: Nonlinear Dynamics and Turbulence, G.I. Barenblatt, G. Iooss and D.D. Joseph, eds. (Pitman, New York 1981), pp. 215–237.
[11] A. Wolf, J.B. Swift, H.L. Swinney and J.A. Vasano, Physica D 16 (1985) 285.
[12] C. Sparrow, The Lorenz Equations: Bifurcations, Chaos and Strange Attractors (Springer, Berlin, 1982).
[13] H.E. de Swart and J. Grasman, Tellus 39A (1987) 10.